Aerophilic Surfaces for Sustained Corrosion Protection of Metals Underwater

Lucia H. Prado, Samer Hayek, Anca Mazare, Ina Erceg, George Sarau, Silke Christiansen, Maksim Kamaleev, Michael Wurmshuber, Ulrich Lohbauer, Wolfgang H. Goldmann, Sannakaisa Virtanen, and Alexander B. Tesler*

Corrosion and biofouling are wetting-related phenomena that limit the effective use of metals in aqueous media. Nonwettable surfaces can mitigate the adverse effects of wetting by minimizing contact with water. However, current achievements in this field fall short of meeting industrial requirements due to the short lifetime of plastrons. This study proposes a method to measure the protective sustainability of plastron. Superhydrophobic (SHS) and aerophilic (APhS) surfaces are constructed on lightweight aluminum and are initially analyzed by conventional goniometry, which show comparable values. However, the plastron that develops underwater is substantially different. While SHS exhibit unevenly broken plastron, APhS show uniform, continuous plastron. As an example of the sustained protective performance of plastron, the corrosion resistance of SHS and APhS is presented. Potentiodynamic polarization, impedance spectroscopy, and long-term immersion in seawater show a drastic enhancement in corrosion resistance, exclusively for APhS. In fact, almost no electrochemical signals are measurable, and no pitting corrosion is observed after 415 days of immersion in seawater. Conversely, SHS show no noticeable improvement and corrode faster than bare Al due to plastron loss. Since goniometric measurements do not provide information on plastron, it is essential to analyze the plastron for any non-wettable surface utilized underwater.

1. Introduction

Development of renewable green energy is essential for future societies to mitigate the climate change crisis by reducing greenhouse gas emissions and enhancing energy reliability. Among the available alternatives, water wave energy is a promising clean energy source that is independent of daylight and is second only to fossil fuels.[1] It has been estimated that the power of waves around the world's coastlines exceeds 2×10^{12} W.[2] Despite decades of research, economic technologies for large-scale water wave energy harvesting are still lacking due to their complex design. In addition, the high cost of deploying and maintaining wave energy systems in harsh aquatic conditions is due to the high corrosiveness and biofouling of surfaces.[3] Therefore, development of lightweight and mechanically robust metallic materials with long-term corrosion and fouling resistance is crucial to meet the

L. H. Prado[+], S. Hayek, A. Mazare, S. Virtanen
Department of Materials Science and Engineering
Institute for Surface Science and Corrosion
Faculty of Engineering
Friedrich-Alexander-Universität Erlangen-Nürnberg
Martensstraße 7, 91058 Erlangen, Germany
I. Erceg, G. Sarau, S. Christiansen
Institute for Nanotechnology and Correlative Microscopy eV INAM
Fraunhofer Institute
Äußere Nürnberger Str. 62, 91301 Forchheim, Germany
G. Sarau, S. Christiansen
Fraunhofer Institute for Ceramic Technologies and Systems IKTS
Äußere Nürnberger Str. 62, 91301 Forchheim, Germany

The ORCID identification number(s) for the author(s) of this article can be found under https://doi.org/10.1002/adfm.202407444

[+]Present address: Fraunhofer Institute for Wind Energy Systems (IWES), Am Haupttor 4310, 06237 Leuna, Germany

G. Sarau
Max Planck Institute for the Science of Light
Staudtstrasse 2, 91058 Erlangen, Germany
S. Christiansen
Institute for Experimental Physics
Freie Universität Berlin
Arnimallee 14, 14195 Berlin, Germany
M. Kamaleev, M. Wurmshuber
Department of Materials Science and Engineering
Chair of General Materials Properties
Friedrich-Alexander-University of Erlangen-Nürnberg
Martensstraße 5, 91058 Erlangen, Germany
U. Lohbauer
Department of Operative Dentistry and Periodontology
Friedrich-Alexander-Universität Erlangen-Nürnberg
91054 Erlangen, Germany
W. H. Goldmann, A. B. Tesler
Department of Physics
Biophysics Group
Friedrich-Alexander-Universität Erlangen-Nürnberg
Henkestrasse 91, 91052 Erlangen, Germany
E-mail: alexander.tesler@fau.de

**ADVANCED
SCIENCE NEWS**

www.advancedsciencenews.com

**ADVANCED
FUNCTIONAL
MATERIALS**

www.afm-journal.de

growing demand for components used in wave energy engineering applications.[4]

However, achieving high corrosion resistance for lightweight metallic surfaces exposed to aqueous media is challenging. Stainless steels have excellent corrosion resistance, but their low strength-to-weight ratio and high price limit their widespread use in certain industrial applications.[5] The most applicable lightweight metallic substitutes to stainless steels are aluminum (Al), titanium (Ti), and magnesium (Mg). While Ti is mechanically durable and corrosion resistant, it is the heaviest, most expensive, and most challenging for machining.[6] Concurrently, Mg is the lightest, but the softness and high activity of its alloys result in elevated levels of wear and corrosion.[7] Furthermore, although Mg offers good machinability, its highly combustible dust presents a significant manufacturing challenge.[8]

Among the available alternatives, aluminum (Al)-based alloys are the widely used structural materials in automotive,[9] aerospace,[10] construction,[11] power transmission,[12] and marine[13] applications due to their light-weight, high strength, easy recyclability, extrudability, and the development of suitable welding techniques for design flexibility.[14] However, their limited corrosion resistance impairs performance and restricts their use under certain conditions. Achieving corrosion resistance comparable to that of stainless steel for lightweight metallic materials such as Al would be beneficial for a sustainable future.

Al is a reactive metal that possesses corrosion resistance due to the presence of an ultrathin native oxide passive film.[15] This native oxide is stable in an aqueous environment in the pH range of ≈4.0–8.5, in that it is easily compromised either in the presence of aggressive anions such as halides or at acidic/alkaline pHs.[16] Generally, Al alloys are divided into two groups according to the mechanism used to adjust their mechanical properties. In the first group, wrought alloys are composed of either a solid solution or dispersion hardening followed by a subsequent treatment of strain hardening. The second group is cast alloys, which are hardened during the casting process and/or heat-treated.[17] However, the corrosion resistance of Al typically decreases when it is alloyed with other elements. The various types of second phases or intermetallic precipitates which are present in such alloys, exhibit different electrochemical properties compared to the Al matrix and typically act as initiation sites for localized (e.g., pitting) corrosion.[18]

Various corrosion protection measures have been established for Al alloys, including surface modification techniques with their particular advantages, but also limitations such as the involvement of hazardous chemicals in some coating approaches.[19] One function of such coatings to achieve corrosion protection is to provide a physical barrier, i.e., to minimize the direct contact of the metallic surface with corrosive media. In this context, wetting-repellent surfaces such as superhydrophobic surfaces (SHS) and liquid-infused porous surfaces have been widely studied for many years as a feasible solution for the protective coating of various metals,[20] and particularly, aluminum.[21] The basic requirement to form SHS is to increase the surface roughness, followed by coating with low surface energy chemicals.[22] The wetting of liquids on rough surfaces has been explained in terms of a balance between the interfacial Gibbs energies of the media involved, i.e., solid, liquid, and vapor[23]; first by Wenzel for the homogeneous wetting regime,

where the liquid completely penetrates the rough grooves,[24] and later by Cassie and Baxter for the heterogeneous wetting, where air is trapped in between the rough protrusions.[25] These two wetting regimes have local minima in the Gibbs energy landscape and often coexist on the same substrate. The Cassie-to-Wenzel transition plays an important role in SHS studies and is the main cause of their failure underwater.[26]

It is common practice to characterize the wettability of solid surfaces by two measures: i) the contact angle (CA) and ii) the roll-off (tilt/sliding) angle. The CA or water contact angle (WCA) in case of aqueous media, quantifies the wettability of a solid surface by a liquid via Young's equation using a goniometer. A surface is usually considered to be superhydrophobic if the advancing WCA is greater than 150° and the roll-off angle is less than 10° (in some references the latter is defined as less than 5°).[27] Here, the macroscopic value obtained by a goniometer is an apparent contact angle.[27] The roll-off angle indicates the angle of inclination at which the drop begins to roll off from the solid surface, while the latter appears to be more conclusive for most SHS.[28] It is closely related to the phenomenon of contact angle hysteresis (CAH),[29] i.e., the existence of a range of metastable CAs ranging from the advancing (maximum) to the receding (minimum) CAs.[30] Most theories and applications to date have focused on the analysis of a water drop on solid surfaces in air, in that surface parameters such as roughness factor and, in particular, entrapped air (also known as plastron) properties such as solid-liquid area fraction, which mainly dictate the stability of SHS,[26a,28,31] are generally not studied and, therefore, not reported for artificial SHS. Another drawback of SHS that should be mentioned is their low mechanical robustness, although this challenge has recently been addressed by several approaches.[32]

To clarify, not all SHS are corrosion resistant, but those with an air plastron, which reduces the contact between the corrosive fluid and the metal substrate. However, it has been demonstrated that plastrons are metastable on engineered SHS.[33] Such metastable performance is significant when SHS are submerged in water, since the air trapped between the rough protrusions diminishes over time,[34] exposing a higher surface area due to increased roughness, ultimately accelerating corrosion.[26b,35] We have recently demonstrated that plastrons can be preserved over years of continuous submersion on special types of SHS, hereafter referred to as aerophilic surfaces (APhS).[36] In addition, APhS have been proven to be effective in inhibiting the attachment of aquatic microorganisms such as bacteria, as well as macro-foulants such as mussels and barnacles.

In this study, we further demonstrate that APhS can dramatically improve the corrosion resistance of metallic samples. We use Al as a representative lightweight metallic substrate because it corrodes easily in aqueous environments. SHS have previously been engineered on Al by etching[37] and anodizing[38] followed by subsequent functionalization with a low surface energy material. In cases, where an improvement in corrosion resistance has been achieved, it has been attributed to air plastron. However, the trapped air layer has not been characterized in detail mainly due to the lack of appropriate characterization techniques. Here, we have systematically developed a process to achieve high Al surface roughness to obtain optimal air plastron without substantial reduction of mechanical properties. For this purpose, a two-step chemical etching process was applied to form
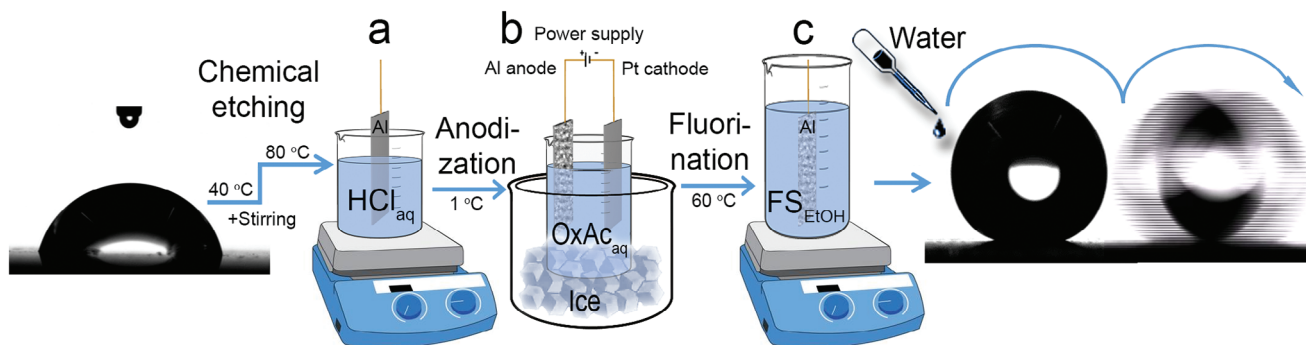
**ADVANCED
SCIENCE NEWS**

www.advancedsciencenews.com

**ADVANCED
FUNCTIONAL
MATERIALS**

www.afm-journal.de

Figure 1. Schematic representation of the EA-Al/FS (aerophilic surfaces) formation process. a,b) The bare Al samples were first chemically modified using the developed two-step etching process to form micro-nanostructures, followed by electrochemical anodization to introduce an additional mesoporous alumina layer. c) The etched/anodized Al samples were then wet chemically modified with the fluorinated surfactant to obtain aerophilic surfaces. The left image shows the water contact angle on the bare Al sample, whilst the right images illustrate the ultra-slipperiness of the aerophilic surfaces as the landed water droplets immediately roll off the surface.

hierarchical micro/nanostructures followed by electrochemical anodization to produce a thin mesoporous oxide layer.[39] The anodization process not only introduces additional nanoscale features and provides a protective oxide layer (in addition to the native, air-formed oxide film), which only partially enhances the corrosion resistance of the substrate but also improves the formation of the fluorinated surfactant coating used to reduce the surface energy of Al. The Al substrates were characterized at each preparation step, first in terms of apparent, advancing, and receding contact angles, and later in terms of surface roughness, and where applicable, air plastron structure and solid-liquid area fraction using optical reflectance microscopy. The combination of etching and anodizing results in a drastically reduced solid-liquid contact area. The APhS, SHS, and control Al samples were tested for corrosion resistance using potentiodynamic polarization curves, electrochemical impedance spectroscopy, and long-term immersion in artificial seawater. Although the conventional goniometric results, i.e., apparent CA, advancing, and receding CAs, revealed comparable wetting characteristics for APhS and SHS, these Al samples displayed contradictory corrosion resistance performance. This distinction is attributed to the air plastron structure, its surface coverage, and therefore, the long-term underwater stability. Thermodynamic stability theory was applied to predict the wetting repellence performance of both SHS and APhS Al samples under water. Therefore, to be sustainable in real-world applications, identification of the plastron structure and subsequent determination of the solid-liquid area fraction should be provided as standard for any engineered SHS and, especially, APhS system.

2. Results and Discussion

2.1. Formation of Superhydrophobic and Aerophilic Surfaces and Their Physicochemical Characterization

Figure 1 schematically shows the process of superhydrophobic/aerophilic coating formation on Al samples. This process was applied to 1000-grade Al substrates ground with SiC abrasive paper to ensure the same initial surface condition for all samples. The typical top-view scanning electron microscopy (SEM) and corresponding atomic force microscopy (AFM) images are

shown in **Figure 2a,b**. The dimensionless (Wenzel) roughness factor, which is the ratio of the actual surface area to the projected (measured) area, was 1.17 ± 0.04. The ground Al samples are referred to as bare Al (B-Al). Note that the procedure described below can be applied equally to polished or rough surfaces regardless of their roughness characteristics. Energy dispersive X-ray spectroscopy (EDS) analysis shows pronounced Al and subtle O peaks, indicating the formation of a thin native aluminum oxide layer (Figure 2g,h).

It is known that Al and its alloys react with HCl by preferentially attacking higher energy sites such as dislocations, grain boundaries, or higher energy crystal orientations, inducing the formation of facetted rectangular pits (crystallographic pit growth).[40] The SEM images of the typical Al sample after one etch step at different temperatures are shown in Figure S1 (Supporting Information). As shown, the size of the rectangular features decreases with increasing etch temperature.

The B-Al samples were immersed in an aqueous 3 M hydrochloric acid (HCl) solution[41] and sequentially etched (two-step etching) for 2 min at 40 °C, followed by 1 min at 80 °C. Due to the strong aggressiveness of the HCl solution, the etched area consists of randomly distributed inhomogeneous rectangular features with a typical size larger than 1 μm after the first etching step. However, to obtain Al-SHS, the roughness must be further improved by forming a hierarchical morphology. A second step was then taken to create a hierarchical structure. Here, the aqueous HCl solution was heated to 80 °C, and the pre-etched Al samples were additionally etched for 1 min. The two-step etched samples are hereafter referred to as E-Al. The SEM and corresponding atomic force microscopy images of the typical E-Al morphology are displayed in Figure 2c,d. As demonstrated, the two-step etching process produces hierarchical micro/nano-scale roughness uniformly distributed over the entire Al sample area (Figure S2a, Supporting Information). The dimensionless roughness parameter was calculated from AFM images and found to be 1.65 ± 0.19 (Figure 2d), which was further confirmed by laser confocal microscopy measurements over a submillimeter area (Figure S2b, Supporting Information).

To form Al-SHS, the E-Al samples were immersed in a 1 wt.% commercial phosphate ester fluorinated alkyl chain surfactant (FS) solution at ambient conditions (Figure S3, Supporting

**ADVANCED
SCIENCE NEWS**

www.advancedsciencenews.com

**ADVANCED
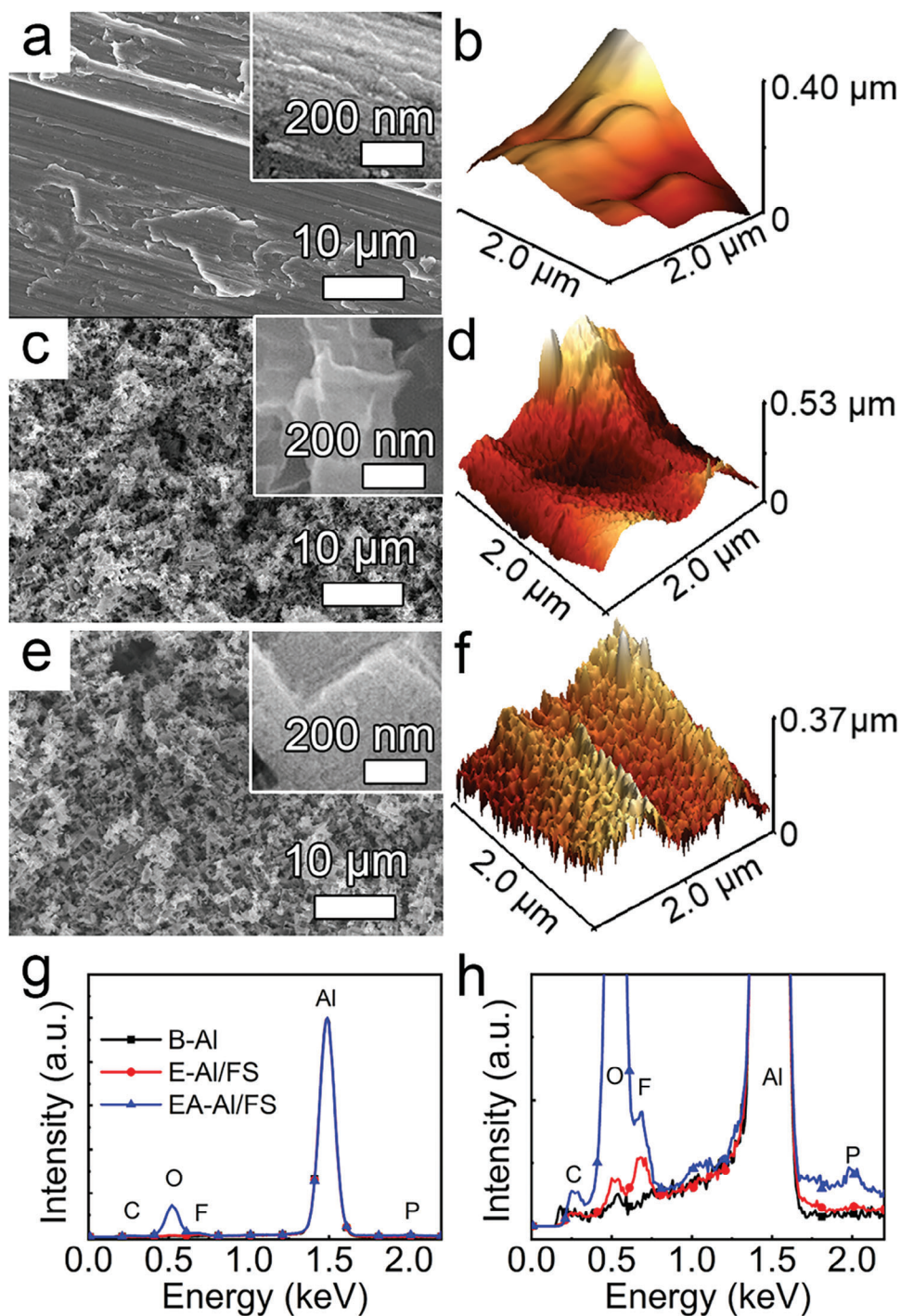FUNCTIONAL
MATERIALS**

www.afm-journal.de

Figure 2. a,b) SEM and corresponding atomic force microscopy images of bare Al surfaces (B-Al), c,d) etched Al surfaces (E-Al), and e,f) etched/anodized Al surfaces (EA-Al). g,h) Corresponding full intensity range and low-intensity area EDS spectra of the bare samples as shown in (a,b), and after the fluorination process of the samples shown in (c,d, e,f).

Information).[32d] Note that poly- and per-fluoroalkyl substances are subject to regulation due to their chemical stability leading to bioaccumulation[42]; thus, their waste should be reduced. The FS solution remained stable for five years with no evidence of degradation in its coating performance, allowing for multiple reuses without waste. Energy dispersive X-ray spectroscopy (EDS) was

used to characterize the chemical composition of the B-Al and E-Al samples after fluorination, referred to as B-Al/FS and E-Al/FS. The results are summarized in Figure 2g,h. As shown, both B-Al/FS and E-Al/FS consist mainly of Al, while carbon (C), oxygen (O), phosphorus (P), and fluorine (F) peaks are hardly seen in B-Al/FS. At the same time, O and F peaks are already observed in
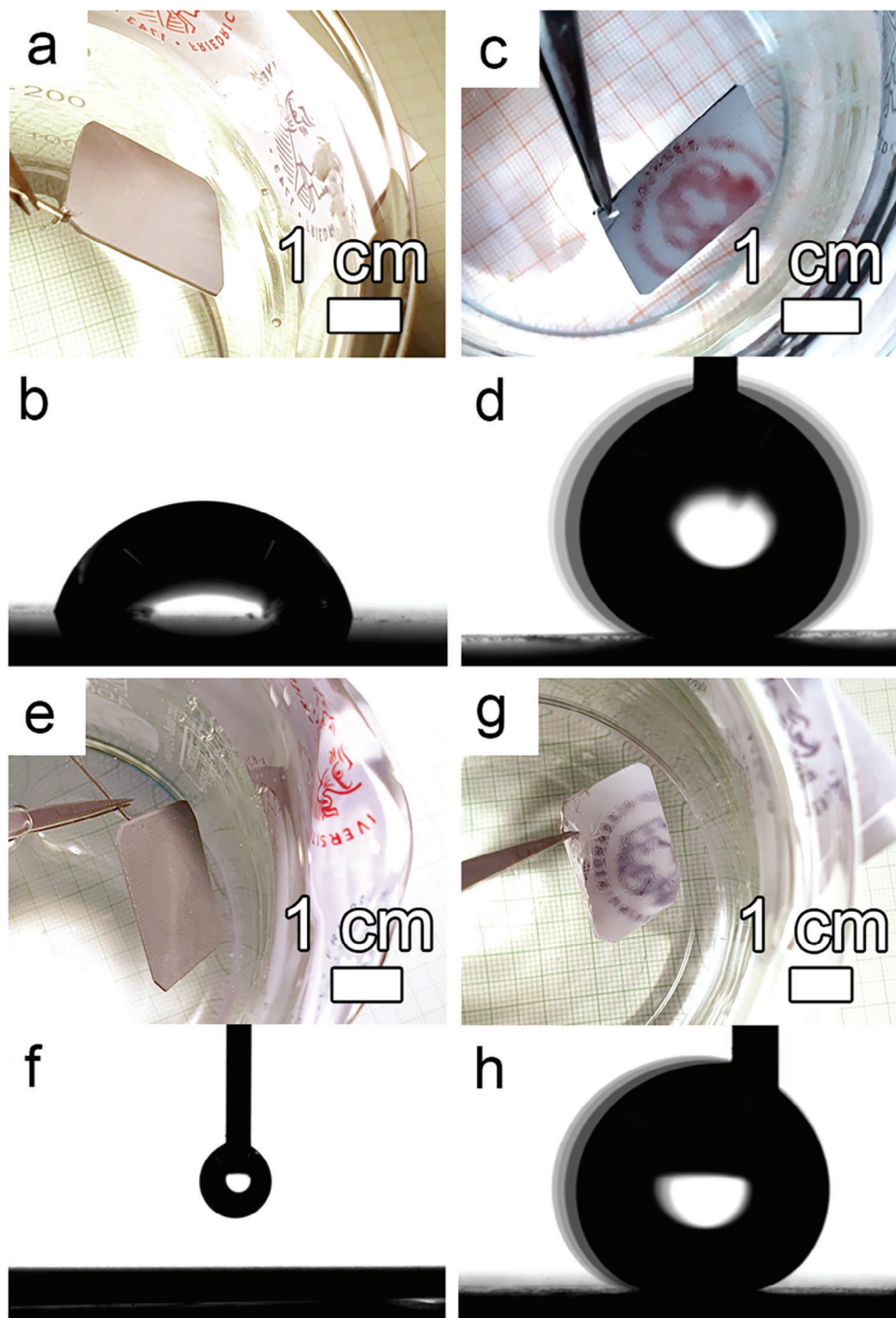
**ADVANCED
SCIENCE NEWS**

www.advancedsciencenews.com

**ADVANCED
FUNCTIONAL
MATERIALS**

www.afm-journal.de

Figure 3. a, c, e, g) Digital images and b, d, f, h) corresponding water contact angles of B-Al (a-b), EA-Al/FS (c-d), EA-Al (e-f), and EA-Al/FS (g-h). The images in (a, c, e, g) were obtained by immersing the samples in a beaker filled with water with the university logo in the background. The images were taken at ≈85° to demonstrate their high reflectance underwater. The images in (d, h) were obtained by overlapping the advancing and receding contact angle images.

the E-Al/FS sample from a self-assembled monolayer of FS. This is due to the increased surface area of the hierarchically structured morphology.

Water contact angle (WCA) measurements were then performed on the B-Al, B-Al/FS, E-Al, and E-Al/FS samples to de-termine their wetting regime. Despite the high reflectance of bare Al, the sample does not show any obvious reflectance underwater (**Figure 3a**). The B-Al samples are hydrophilic with a WCA of $74.0° \pm 0.2°$ (Figure 3b). Note that Al is considered a high surface energy material with a low WCA due to the

**ADVANCED
SCIENCE NEWS**

www.advancedsciencenews.com

**ADVANCED
FUNCTIONAL
MATERIALS**

www.afm-journal.de

formation of a native oxide layer.[43] This relatively high WCA is due to airborne hydrophobic contaminants, which is consistent with the literature.[43b,44] While functionalized with FS, the WCA of B-Al/FS increases to 148.6° ± 2.1° (Figure S4, Supporting Information).

The freshly prepared E-Al samples showed a WCA of 2.6° ± 2.4°, i.e., almost complete wetting of the Al surface due to the increased surface roughness (Movie S1, Supporting Information). After FS functionalization, the E-Al/FS samples are highly reflective when immersed in water, indicating the formation of air plastron (Figure 3c). The water drops deposited on the E-Al/FS surface rolled off rapidly making it difficult to measure the apparent CA by conventional goniometry (see Movie S2, Supporting Information). Therefore, the advancing (θ_{Adv}) and receding (θ_{Rec}) CAs were measured, and the results are summarized in Figures 3d and 4a, Figure S5 and Movie S3 (Supporting Information). Note that the Ellipse model was used to calculate the θ_{Adv} and θ_{Rec} with the needle inserted in a water drop,[45] while the fitted values are always lower than those achieved by the Laplace–Young model.[46] Therefore, only the difference between the θ_{Adv} and θ_{Rec} should be considered, not the fitted values. As demonstrated, there are only insignificant (if any) differences between the θ_{Adv} and θ_{Rec}. Although the first derivative (ΔWCA), which represents the change in the fitted apparent CA values during the infusing and withdrawing steps, shows higher deviations (**Figure 4a**, lower plot), the E-Al/FS surfaces show very low water drop adhesion (Figure S5, Supporting Information). Considering the wetting measurements, we can conclude that the E-Al/FS surfaces are in the Cassie–Baxter (heterogeneous) wetting regime, i.e., the deposited drop is only partially in contact with the solid surface, and the rest is in contact with the air trapped in the grooves.

The shape of the air plastron was determined using bright-field optical reflectance microscopy imaging on the E-Al/FS samples immersed in water.[36] Plastron on E-Al/FS samples prepared under various conditions, i.e., one- and two-step etching processes, has an uneven, broken shape (Figure 4c; Figure S6, Supporting Information). The plastron coverage, i.e., the solid-liquid area fraction, of E-Al/FS samples was estimated from the optical microscopy images and was found to be 75.3 ± 3.2% (i.e., darker gray area). The latter confirms a heterogeneous (Cassie–Baxter) wetting regime of the E-Al/FS samples, but the solid-liquid area fraction, i.e., the actual number of pinning points, where the deposited water droplet contacts the solid surface, is still high. This unevenly ruptured plastron explains the higher deviations in ΔWCA values, i.e., there is no uniformity of the plastron layer with more pinning states. The relatively high value of the solid-liquid area fraction can be attributed to the low coverage of the surface by the FS monolayer due to the insufficient amount of Al oxide/hydroxide required to react with the phosphate ester (Figure 2g,h).[15,47] Note that for the E-Al/FS samples, the EDS oxygen peak originates from both the native alumina and the fluorinated phosphate ester.

Therefore, to improve the quality of the self-assembled FS monolayer as well as to introduce additional fine nanoscale roughness, an electrochemical anodization step was employed. The pre-etched (E-Al) samples were anodized in an aqueous oxalic acid electrolyte.[48] The typical anodized E-Al surface is shown in Figure 2e,f and Figure S7 (Supporting Information). The an-

odized E-Al samples are referred to as EA-Al. As shown, anodization introduces additional roughness to the hierarchical rectangular features through the formation of an anodic aluminum oxide layer and the incorporation of carboxylate species from the anodizing electrolyte (Figure S8a, Supporting Information),[49] in that the EDS analysis confirms the formation of the oxide layer on EA-Al samples (Figure S8b,c, Supporting Information). Corresponding AFM measurements showed a dimensionless roughness factor of 3.63 ± 0.15. Note that it is difficult to measure roughness on such high surface area samples. We have previously shown that AFM provides the lowest roughness values among available alternatives measuring surface roughness.[36a] The EA-Al samples are of gray color at very low reflectivity under water due to high roughness with complete wetting, i.e., below the goniometer's ability to measure WCA (Figure 3e,f; Movie S4, Supporting Information).

When functionalized with FS, the SEM image demonstrates a similar morphology, whilst the EDS analysis reveals pronounced C, F, and P peaks, confirming the successful formation of a self-assembled monolayer of the FS (Figure 2g,h).[32d] Again, the dripping water drops roll off rapidly, whilst smaller volume drops do not adhere to the EA-Al/FS surface, both of which make it difficult to measure the apparent CA by goniometric measurements (Movie S5, Supporting Information). While non-reflective in air, the EA-Al/FS samples show a perfect mirror-like reflection while immersed underwater, confirming the existence of air plastron (Figure 3g). The advancing and receding CAs were measured and showed negligible differences (Figures 3h and 4b; Movie S6, Supporting Information). To compare the air plastron shape, the FS functionalization was applied to samples prepared by various two-step etching processes followed by the standard anodization procedure, although all these samples displayed air plastron shape and coverage similar to E-Al/FS (Figure S9, Supporting Information). In contrast, plastron on EA-Al/FS samples is continuous (light gray-colored area) with round-shaped pinning points (dark spots) evenly distributed over the entire area (Figure 4d). In addition, the first WCA derivative of the EA-Al/FS samples shows a much smoother signal, indicating that the change in drop shape during the infusion and withdrawal of the drop is minimal due to the continuous plastron, meaning almost frictionless condition (Figure 4b, lower part). The solid-liquid area fraction was calculated from the bright-field optical reflection microscopy images and was found to be 16.0 ± 7.9%, i.e., four times lower compared to E-Al/FS. The latter means that, on average, ≈16% of the solid substrate is in direct contact with the aqueous medium, again emphasizing the significance of the hierarchical morphology.

Considering the solid-liquid area fraction and the roughness parameter, the thermodynamic stability of the plastron underwater can be estimated according to the following equation[50]:

$$r > \frac{-1}{\cos(\theta)} + \varphi_s \left(1 + \frac{1}{\cos(\theta)}\right) \equiv r_{min} \tag{1}$$

where θ is the Young's CA (estimated with the most stable CA, MSCA), r is the dimensionless roughness, and φ_s is the solid-liquid area fraction. Here, the minimum value of the roughness ratio required to achieve stable superhydrophobicity at a given φ_s should be greater than r_{min}. To measure the MSCA, the 100 nm thick SiO_2 layer on a polished Si wafer was used. This is because
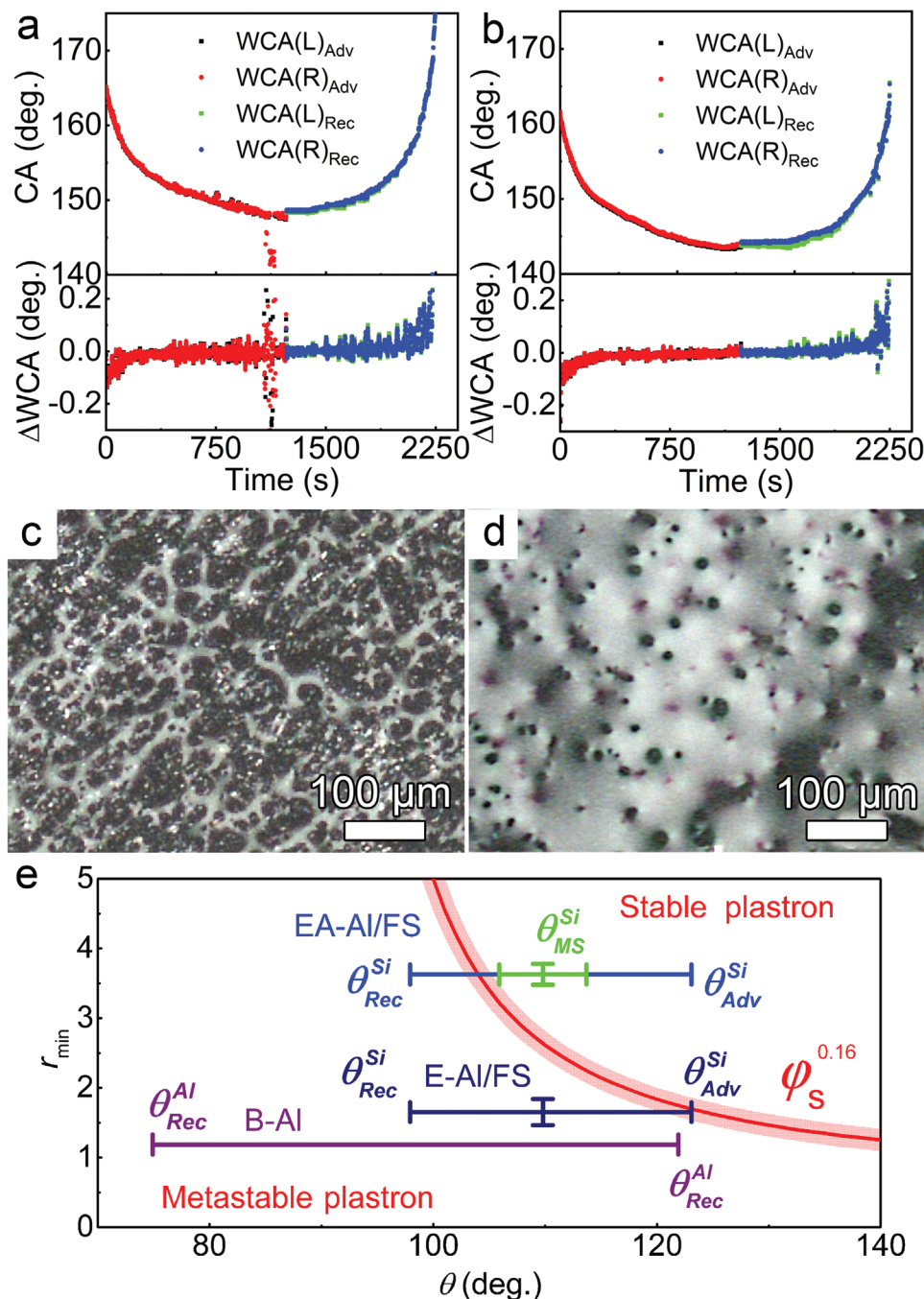
Figure 4. a,b) Advancing and receding contact angle (hysteresis) measurements of (a) E-Al/FS, and (b) EA-Al/FS surfaces. The Ellipse model was used to obtain the WCA values. The abbreviations *R* and *L* refer to the right and left water contact angles, while *Adv* and *Rec* refer to the advancing and receding water contact angles, respectively. Bright-field optical reflectance microscopy images of the E-Al/FS (c), and EA-Al/FS (d) surfaces immersed in water. e) The Marmur diagram of the thermodynamic stability of plastron underwater was calculated for EA-Al/FS samples, and B-Al/FS and E-Al/FS for comparison.

it is challenging to obtain Al with nanometer roughness, in that it has been shown that topographical defects with a lateral extent of less than 1 nm are sufficient to induce a measurably large CAH.[51] The MSCA ($\theta^{Si}_{MS} = 109.8° \pm 3.9°$) measurements represent an average of apparent CAs on a given smooth surface of the same hydrophobic origin, meaning the same fluorinated sur-

factant, measured by the advancing ($\theta^{Si}_{Adv} = 122.6° \pm 1.4°$) and receding ($\theta^{Si}_{Rec} = 97.0° \pm 3.6°$) WCAs.[27] When combining the measured roughness and the solid-liquid area fraction with the MSCA, the plastron stability can be estimated.[36a] Considering the high solid-liquid area fraction values of E-Al/FS (Figure 4e, dark blue), these samples do not fulfill the basic requirement

of the thermodynamic stability model, i.e., the wetting liquid only touches the top of the rough asperities without penetrating into the grooves.[50] This is attributed to the low surface coverage of the FS on the etched Al samples due to the lack of oxide/hydroxide groups, i.e., these samples are superhydrophobic but not aerophilic (Figure 2g,h; Figure S10 and Table S1, Supporting Information). On the contrary, the calculations suggest that the EA-Al/FS substrates exhibit a thermodynamically stable plastron, i.e., aerophilic surfaces with a stable Cassie–Baxter wetting regime (Figure 4e, blue). The significance of this information in predicting the wetting-related performance of SHS and APhS, such as corrosion resistance in terms of efficiency and lifetime, will be demonstrated in the following sections.

2.2. Mechanical Durability

To ensure the longevity of water-repellent performance, SHS/APhS should be mechanically durable to withstand physical stresses such as abrasion, bending, or impact without losing functionality and performance. As discussed previously, non-wettable surfaces typically exhibit hierarchical micro/nanoscale structures that can be damaged or altered by mechanical stresses.[32d] Therefore, for practical applications, where SHS/APhS may be exposed to mechanical wear and tear, but also in under water applications with elevated hydrostatic pressure, it is essential to sustain their mechanical durability. Here, nanoindentation was applied to characterize the developed SHS and APhS, along with bare Al samples, to gain insight into their mechanical properties. The results of the nanoindentation measurements are summarized in **Figure 5**.

As shown in Figure 5a, the bare and rough Al samples exhibit a comparable hardness of ≈0.5–0.7 GPa indicating that the surface modifications of the E-Al and EA-Al samples do not deteriorate their mechanical characteristics. In the case of EA-Al, the hardness is slightly higher than that of bare Al due to the formation of the ceramic mesoporous aluminum oxide layer.[52] The elastic modulus of both E-Al and EA-Al samples is ≈30–35 GPa, which is about half of that of the bare Al samples (66 GPa) (Figure 5b). The decrease in elastic modulus is attributed to the formation of a porous structure on the surface of E-Al and EA-Al. Nevertheless, the elastic modulus of these samples remains in the gigapascal range, providing a stiff and durable surface for their applications.

2.3. Potentiodynamic Polarization

Figure 6a shows potentiodynamic polarization curve measurements carried out in an aqueous electrolyte containing 3.5 wt.% NaCl, the standard concentration used to simulate seawater chloride concentration. The B-Al curve shows a short passive range followed by the breakdown of passivity upon anodic polarization with pitting corrosion spreading over the entire surface with an I_{corr} of 2.13×10^{-1} µA cm^{-2} and an E_{corr} of -0.807 V$_{Ag/AgCl}$ (Figure 6a,b). The same substrates coated with FS show a more noble E_{corr} of -0.782 V$_{Ag/AgCl}$ and a significantly lower current density in the cathodic branch due to the protective nature of the FS-covered surface,[15] resulting in an I_{corr} value of 7.43×10^{-2} µA cm^{-2}. However, upon anodic polarization, active dissolution is observed with only slightly reduced anodic
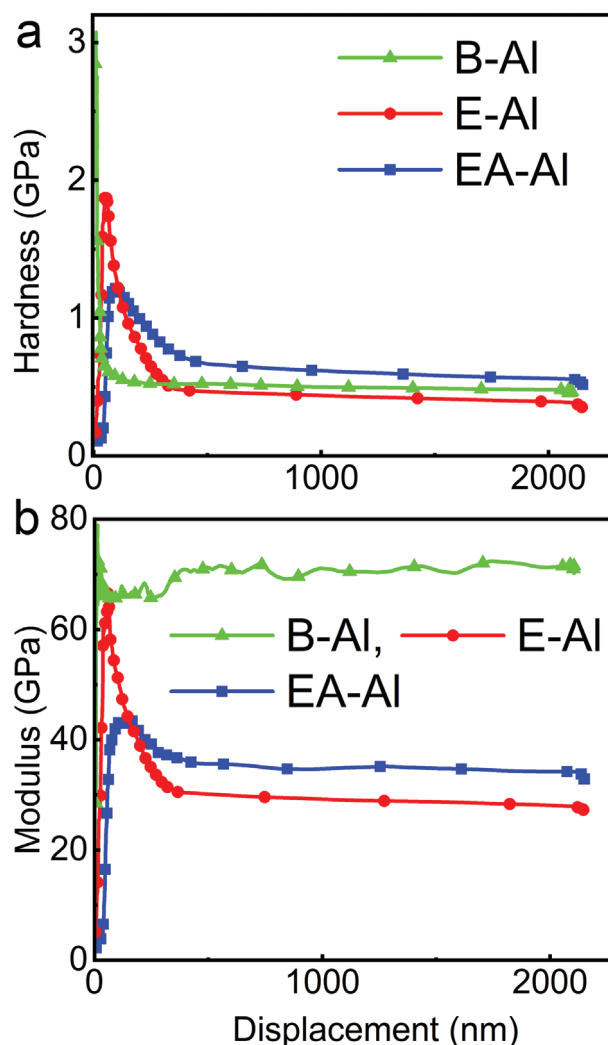

Figure 5. a) Hardness and b) elastic (Young's) modulus as a function of nanoindenter penetration depth. Data represent the average of at least six independent indentations.

current densities as compared to the B-Al surface. As shown in Figure 6a,c, the attack was unevenly distributed over ≈30% of the exposed sample test area. When etched, the E-Al samples show a more positive E_{corr} value of -0.777 V$_{Ag/AgCl}$, but the corrosion current density was significantly higher (4.13 µA cm^{-2}) due to the increased surface area of these samples. Optical microscopy and digital images show localized corrosion, with unevenly distributed attack coverage over ≈50% of the exposed surface (Figure 6a,d). After functionalization with FS, meaning Al-SHS, the E-Al/FS shows a comparable current density and corrosion potential (3.76 µA cm^{-2} and -0.751 V$_{Ag/AgCl}$, respectively) to that of the E-Al, but the sites of localized attack cover ≈11% of the test area (Figure 6a,e).

When etched and anodized, the E_{corr} of the EA-Al sample increases even more to up to -0.769 V$_{Ag/AgCl}$ with a corrosion current density of 4.14 µA cm^{-2}. In addition, in the anodic region, the current density is lower than for the previous samples until ≈0.0 V$_{Ag/AgCl}$, indicating that the mesoporous Al

**ADVANCED
SCIENCE NEWS**

www.advancedsciencenews.com

**ADVANCED
FUNCTIONAL
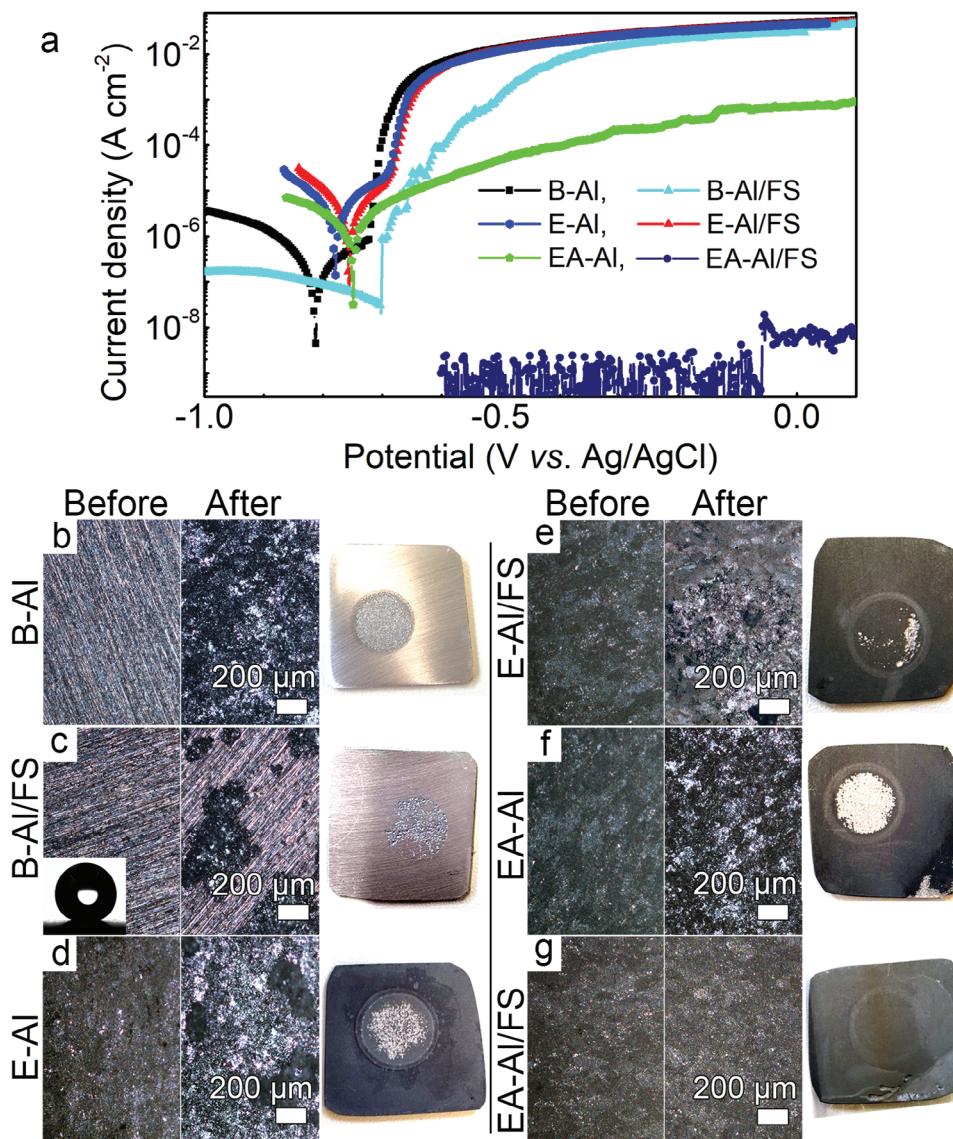MATERIALS**

www.afm-journal.de

Figure 6. a) Potentiodynamic polarization curve measurements and b–g) bright field optical microscopy and digital still images of B-Al (b), B-Al/FS (c), E-Al (d), E-Al/FS (e), EA-Al (f), and EA-Al/FS (g) before and after potentiodynamic polarization, measured in a 3.5 wt.% NaCl aqueous electrolyte. Inset in (c) is the water contact angle measurement. The magnification of the optical microscopy images before and after the experiment is identical for all images.

oxide layer with the nanoscale features provides some additional corrosion protection, although at extended polarization the surface undergoes massive dissolution covering ≈70% of the surface (Figure 6a,f).

The greatest improvement in the corrosion resistance was observed for the EA-Al/FS samples (Al-APhS). In this case, the current in the polarization curve starts to increase only ≈0.0 $V_{Ag/AgCl}$ and still maintains values significantly lower than all the samples previously mentioned (Figure 6a). It is important to note that no localized corrosion or any type of degradation was observed on the surface of the EA-Al/FS samples even after reaching a high potential such as +1.5 $V_{Ag/AgCl}$ at the end of the experiment (Figure 6a,g; Figure S11, Supporting Information). The noisy current signal over the entire potential range for this sample indicates poor contact of the electrolyte with the sample surface. The EA-Al/FS sample still shows a high and continuous reflectivity over the whole sample area after the potentiodynamic polarization measurement when re-immersed in water (**Figure 7a**), i.e., there is no difference between the corrosion-exposed and unexposed outer areas, which is also confirmed by the advancing and receding CA measurements (Figure 7b; Movie S7, Supporting Information). The potentiodynamic polarization results are summarized in **Table 1**. The comparison between the corrosion resistance of the E-Al/FS (SHS) and EA-Al/FS (APhS) samples emphasizes that i) plastron retards the development of localized forms of corrosion, and ii) it is only useful in the case where plastron completely covers the sample surface.
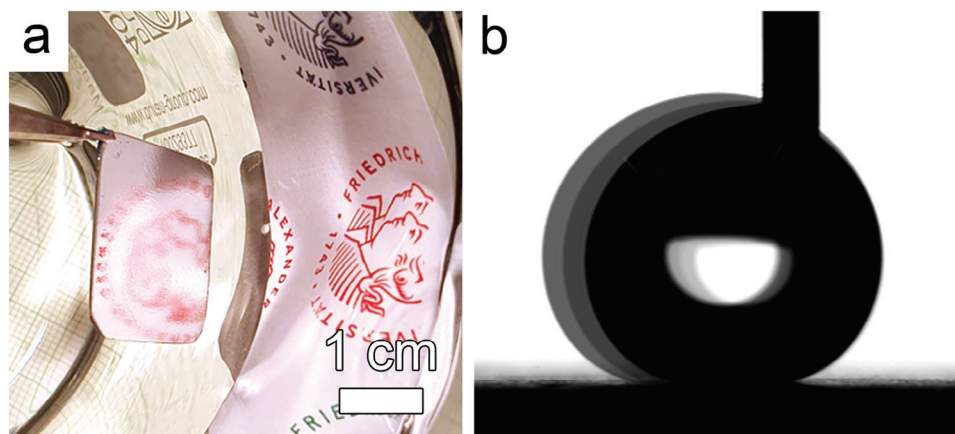
**ADVANCED
SCIENCE NEWS**

www.advancedsciencenews.com

**ADVANCED
FUNCTIONAL
MATERIALS**

www.afm-journal.de

Figure 7. a) Digital still image and b) corresponding water contact angle hysteresis of the EA-Al/FS sample after potentiodynamic polarization measurements. The image in (a) was obtained by immersing the sample in a beaker of water and the image was taken at an angle of ≈85°. The CAH in (b) was measured at the corroded area, and the image was created by overlapping the advancing and receding contact angle frames.

2.4. Electrochemical Impedance Spectroscopy

Electrochemical impedance spectroscopy (EIS) is a non-destructive technique commonly used to characterize the electrochemical performance of an interface. **Figure 8a** shows the Bode impedance modulus plot of the developed surfaces. As shown, the B-Al, E-Al, and EA-Al surfaces have impedance modulus values of 155.0, 196.5, and 177.9 Ω cm^2, respectively, at the high-frequency end of 10 kHz, while the E-Al/FS and EA-Al/FS surfaces have modulus values of 2.21×10^3 and 7.79×10^4 Ω cm^2, respectively, which are 11 and 400 times higher than the non-FS-functionalized samples at the same frequency. While the high-frequency modulus of the first three samples reflects the resistance of the electrolyte solution, the latter two samples fail to do so, which is most likely due to a low capacitance (CP) element coupled to the interfacial performance. Similarly, at a low frequency of 0.1 Hz, the modulus values of E-Al/FS and EA-Al/FS are 2.33×10^6 and 1.94×10^9 Ω cm^2 compared to 2.41×10^5, 9.92×10^3, and 1.24×10^5 Ω cm^2 for B-Al, E-Al, and EA-Al, respectively. At the low-frequency limit, the modulus is related to the charge transfer resistance and the double-layer capacitance.[53] The higher impedance modulus in the low-frequency range indicates better corrosion resistance of the FS-functionalized surfaces,[54] whilst the increase in the impedance modulus of the EA-Al/FS (APhS) sample is attributed to the nearly continuous air plastron (barrier) layer

that effectively prevents the electrolyte from reaching the Al substrate surface.

Figure 8b shows the Bode phase angle diagram of the developed surfaces. The B-Al and E-Al samples show one time constant in the low-frequency range related to the metal substrate, while the EA-Al sample has two time constants; the higher frequency one being associated to the protective coating.[53] The E-Al/FS sample shows a time constant in the high-frequency range and then reaches a plateau around a phase angle of −53°. The data for the EA-Al/FS (APhS) sample are scattered and noisy over the measured frequency range due to the very high resistivity of the coating.

The EIS curves were further simulated, where possible, by equivalent circuit elements used to represent the performance of various interfaces and media in the developed surfaces. The resistance of the electrolyte solution is denoted as R_s. A single time constant in the B-Al and E-Al samples represents the charge transfer resistance (R_{ct}) and the capacitance associated with the double layer present at the interface between the solid surface and the electrolyte (Figure 8, black and red curves; Figure S12a and Table S2, Supporting Information). The latter is modeled by a constant phase element (CPE_{dl}), which indicates the imperfection of the solid surface, i.e., a nonideal performance that is attributed to surface roughness and irregularities in surface termination, porosity, etc.[55] The EA-Al sample exhibits an additional time constant representing the resistance (R_{ox}) and capacitance (CPE_{ox}) due to an anodic Al oxide layer (Figure 8, cyan curves; Figure S12b and Table S2, Supporting Information). When functionalized with FS (Al-SHS), the coating is represented by R_{FS}, while the surface is partially covered either by air or in contact with the electrolyte. This partial plastron coverage is represented by the additional time constant components of resistance (R_{air}) and capacitance (CPE_{air}) connected in parallel with R_{ct} and CPE_{dl} (Figure 8, green curves; Figure S12c and Table S2, Supporting Information). Here, the bilayer capacitance deviates significantly from the ideal, while R_{air} and R_{FS} are both in the order of hundreds of MΩ cm^2, indicating a high efficiency of the protective coating (Table S2, Supporting Information). The EA-Al/FS (APhS) curve could not be simulated due to a very large scatter in

Table 1. Corrosion current density and corrosion potentials were calculated from the Tafel plots as shown in Figure 6a.

Sample	I_{corr} [μA cm^{-2}]	E_{corr} [V$_{Ag/AgCl}$]
B-Al	2.13×10^{-1}	−0.807
B-Al/FS	7.43×10^{-2}	−0.782
E-Al	4.13×10^{0}	−0.777
E-Al/FS	3.76×10^{0}	−0.751
EA-Al	4.14×10^{0}	−0.769
EA-Al/FS	–	–

**ADVANCED
SCIENCE NEWS**

www.advancedsciencenews.com

**ADVANCED
FUNCTIONAL
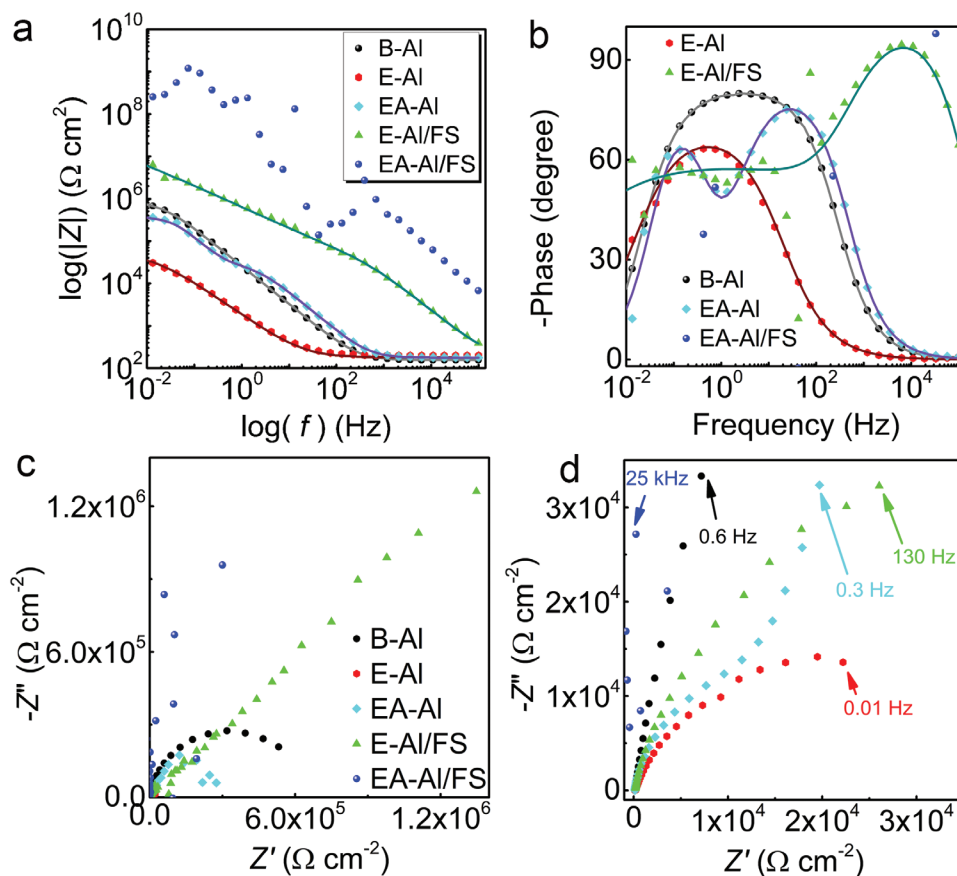MATERIALS**

www.afm-journal.de

Figure 8. Electrochemical impedance spectroscopy measurements of the B-Al, E-Al, E-Al/FS, EA-Al, and EA-Al/FS surfaces. Bode plots of a) impedance modulus |Z|, b) phase angle versus frequency, c) Nyquist plots, and d) their zoom-in view in the high-frequency region. The solid lines in (a-b) represent the fitted equivalent circuit impedance. The EIS data were measured in an aqueous borate electrolyte.

the measured data, especially in the low-frequency range, again indicating the hindrance of charge transport toward the metal surface (Figure 8, blue curves; Figure S13, Supporting Information).

2.5. Long-Term Immersion in Artificial Seawater

Finally, to investigate the long-term stability and corrosion protection of the plastron on Al-APhS, the EA-Al/FS samples were immersed in artificial seawater for several weeks, while E-Al/FS (Al-SHS) and B-Al were used as control. The results of long-term immersion in seawater are summarized in **Figure 9** and Figures S14–S16 (Supporting Information). The B-Al samples were shiny and reflective at the beginning of the experiment (Figure 9a). After 3 weeks of immersion, pits were formed and the surface turned grey (Figure S14, Supporting Information). After 5 weeks, the surface of these samples turned brown (Figure 9b). In addition, white Al oxide/hydroxide corrosion products were observed floating in the water and settling to the bottom of the Petri dish and samples (Figure S14c, Supporting Information, lower inset). After 20 weeks of immersion, the B-Al samples are severely corroded with white Al oxide/hydroxide precipitates on their surface (Figure S14, Supporting Information, bottom inset). The

E-Al/FS (Al-SHS) samples corrode already severely within one day of immersion in artificial seawater (Figure 9c,d). This is because the plastron on these samples is rapidly lost, exposing a high metallic surface area with low FS coverage to the corrosive medium (Figure 9c,d, lower inset images). A layer of patchy Al oxide/hydroxide precipitates spread over the entire Petri dish after 16 days of immersion (Figure S16a, Supporting Information), while all Al-SHS samples exhibit severe corrosion after 120 days (Figures S15e and S16b–d, Supporting Information).

In the case of EA-Al/FS (APhS), neither corrosion-induced color change nor white Al oxide/hydroxide precipitation were observed after 13 months (415 days) of continuous immersion (Figure 9e,f; Figures S14b and S15d,f, Supporting Information). The latter is more than 8 times longer than previously predicted for the infinite plastron lifetime in deionized water.[56] As shown in Figure 9f, lower inset image, these samples exhibit mirror-like reflectance underwater during the immersion period indicating the presence of trapped air that effectively separates the Al surface from direct contact with the corrosive seawater (Figure S14, Supporting Information, bottom insets). This immersion experiment supports our hypothesis that the corrosion resistance of metallic APhS is enhanced due to i) the thermodynamically stable and continuous plastron underwater, which eliminates direct contact of the highly corrosive media with the Al surface, and ii)
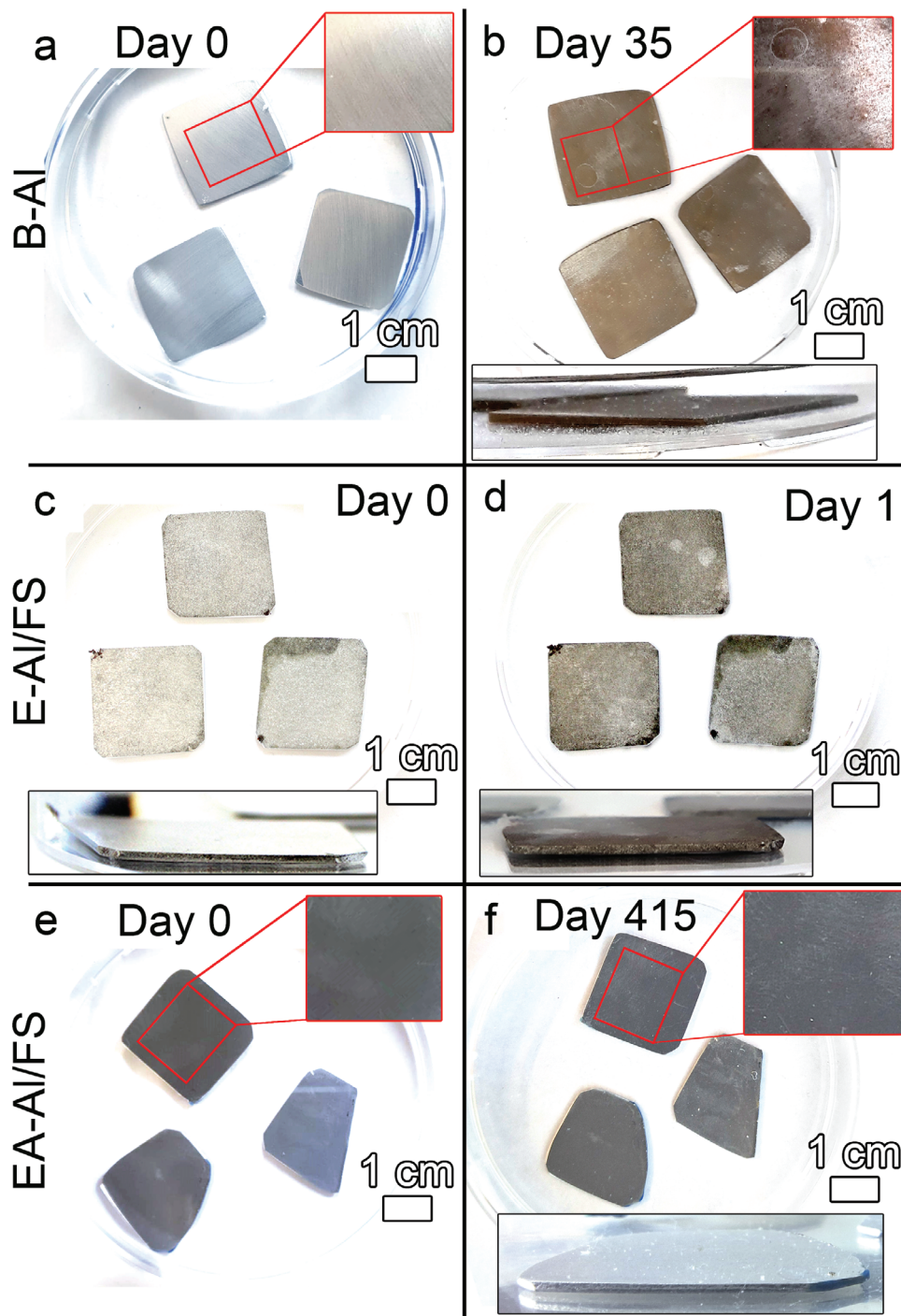
Figure 9. a, c, e) Digital images of the B-Al, E-Al/FS, and EA-Al/FS samples at day 0 of immersion in artificial seawater. b) The B-Al samples after ≈5 weeks of immersion in artificial seawater. d) The E-Al/FS samples after 1 day of immersion in artificial seawater. f) The EA-Al/FS samples after more than 13 months (415 days) of immersion in artificial seawater medium. The inset images in (a-b, e-f) are the magnified surface of the sample marked by the red square. The bottom images in (b-d, f) are taken at a grazing angle to the sample surface to demonstrate alumina precipitates (b), the disappearance of plastron (c-d), and the reflectivity of plastron underwater (f).

ADVANCED
SCIENCE NEWS
www.advancedsciencenews.com

ADVANCED
FUNCTIONAL
MATERIALS
www.afm-journal.de

the FS coating along with the mesoporous alumina layer delay the onset of Al corrosion at the pinning points.[15]

3. Conclusions

This study demonstrates a means to fabricate aerophilic surfaces (APhS) with continuous air plastron underwater. A two-step chemical etching followed by an electrochemical anodization process was developed to form hierarchically rough Al surfaces. The resulting Al substrates were then wet functionalized with fluorinated phosphate ester to reduce their surface energy. The Al surfaces were characterized in terms of their wetting regime after each of the steps, i.e., i) the two-step chemical etching followed by ii) the electrochemical anodization. In both cases, after surface fluorination, the apparent WCA was difficult to measure using conventional goniometry because the water drops rapidly rolled off from these surfaces, while the advancing and receding CA values were also comparable showing only minor differences. Moreover, on the macrometer scale, both SHS and APhS showed similar reflectance under water due to the air plastron obtained by digital camera imaging. Despite the similarity of the WCAs, the shape of the air plastron and its surface coverage differ substantially between the etched (E-Al/FS, SHS) and etched/anodized (EA-Al/FS, APhS) substrates functionalized with the fluorinated surfactant. While the air plastron on the E-Al/FS samples has an uneven, broken shape with a solid-liquid area fraction as high as 75% indicating superhydrophobicity of these samples, the EA-Al/FS samples show an almost continuous air plastron with only 16% of evenly distributed round pinning points, meaning the liquid touches the tops of the rough asperities only, i.e., the aerophilic surface.

The Al samples of both types, i.e., SHS and APhS, were tested for their corrosion resistance in a 3.5 wt.% NaCl aqueous electrolyte as well as by long-term immersion in artificial seawater. A significant difference in the corrosion resistance of the E-Al/FS (SHS) and EA-Al/FS (APhS) surfaces was observed despite similar apparent, advancing, and receding WCAs. It should be emphasized that, if only WCA and CAH measurements are considered, these surfaces would be expected to have nearly identical corrosion resistance. This is because WCA/CAH measurements provide neither unambiguous information about the plastron nor indicate the effectiveness of the corrosion protection (Figure S17, Supporting Information); thus, they can only be used for the first screening of the developed SHS. While the potentiodynamic polarization curves of the E-Al/FS (Al-SHS) samples showed only a slight improvement over B-Al and B-Al/FS, the corrosion current density of the EA-Al/FS (Al-APhS) was inhibited by up to 7 orders of magnitude compared to E-Al/FS due to the formation of a continuous air plastron (i.e., dielectric barrier layer) that effectively eliminates direct contact between the corrosive electrolyte and the Al substrate. In addition, the FS coating along with the mesoporous alumina layer, further protect Al from corrosion at the pinning points. The results obtained from the potentiodynamic polarization curves were confirmed by electrochemical impedance spectroscopy measurements, suggesting the hindrance of charge transport toward the metal surface. Long-term immersion of EA-Al/FS (APhS) samples further confirms the beneficial role of the thermodynamically sta-

ble plastron, in that APhS samples showed a largely corrosion-free surface even after more than 13 months of continuous immersion in seawater media. In contrast, E-Al/FS (Al-SHS) samples with comparable WCA and CAH values corrode severely already within one day of immersion in artificial seawater due to the rapid loss of plastron and the exposure of its high Al surface area to the corrosive medium. The latter confirms that such high metallic surface area samples corrode even faster compared to the bare Al. Therefore, as a standard for underwater applications, in view of the corrosion protection efficiency of non-wettable coatings such as superhydrophobic and, particularly, aerophilic, it is crucial to determine and report on the structure, shape, and surface coverage of the plastron in addition to goniometric measurements, which provide only indirect and limited information. To be applicable, the non-wettable surface technology should be further characterized in terms of water temperature, hydrostatic pressure, and hydrodynamic stability. These factors would influence the shape and surface coverage of the plastron, thus affecting its underwater stability. Yet, obtaining such dependence is still a challenge due to the lack of existing characterization techniques and thermodynamic theories, while this research demonstrates the beneficial role of plastron under water.

4. Experimental Section

Materials: Aluminum 1000-grade sheets of 1 mm thickness (99.5% Al) were purchased from Advent Research Materials, UK. Hydrochloric and oxalic acids were purchased from Sigma–Aldrich, Germany, and ethanol, acetone, and toluene were purchased from Carl Roth, Germany, and used as received. Deionized water (DI) with a resistivity of 18.2 MΩ cm was used in all experiments.

Two-Step Aluminum Etching Process: Aluminum sheets were cut into $20 \times 20 \times 1$ mm samples and used as substrates. The substrates were first ground with SiC grinding paper up to 1200 grit. The substrates were then ultrasonically degreased in acetone and ethanol for 10 min each and dried under a stream of N_2. The ground Al samples were pretreated in an aqueous solution of 1 M NaOH for 1 min, followed by a desmutting treatment in an aqueous solution of 1 M HNO_3 for 1 min at room temperature under stirring conditions,[57] then rinsed with DI water and dried under a stream of N_2. These samples are referred to as B-Al. The B-Al samples were etched in an aqueous solution of 3 M hydrochloric acid, first at 40 °C for 2 min, followed by a second etching step at 80 °C for 1 min under stirring conditions, rinsed with DI water, and then dried under a stream of N_2. The Al samples after the two-step etching process are referred to as E-Al.

Aluminum Anodizing Process: The E-Al samples were further electrochemically anodized in an aqueous solution of 0.3 M oxalic acid maintained at 1 °C for 1 min under an applied voltage of 60 V to form a nano-rough Al oxide layer. A two-electrode cell was used with Pt foil as the counter electrode. The distance between the counter and working electrodes was kept at ≈10 mm. After anodization, the substrates were rinsed with DI water and then dried under a stream of N_2. The E-Al samples after the anodizing step are referred to as EA-Al.

Preparation of Superhydrophobic Coating: The 1 wt.% fluorinated surfactant FS-100 was dissolved in 1 L of 95:5 vol% ethanol:H_2O by ultrasonication and then kept in a closed container at ambient conditions. The B-Al, E-Al, and EA-Al samples were immersed in a container containing the FS solution with a plastic cover used to prevent ethanol evaporation. A container holding the samples was placed in a muffle furnace preheated to 60 °C for 30 min. The low surface energy Al substrates were then removed from the FS solution, rinsed with ethanol, and dried under a stream of N_2. The FS-functionalized Al samples are referred to as B-Al/FS, E-Al/FS, and EA-Al/FS.

**ADVANCED
SCIENCE NEWS**

www.advancedsciencenews.com

**ADVANCED
FUNCTIONAL
MATERIALS**

www.afm-journal.de

Morphology and Physicochemical Characterization: A field emission scanning electron microscope (Hitachi FE-SEM S4800) equipped with an energy-dispersive X-ray spectrometer (Genesis, Oxford Instruments) was used for morphological characterization. The plastron shape and the solid-liquid area fraction of the SHS Al samples were obtained using a Nikon Eclipse LV 150 microscope equipped with a Nikon DS-Fi1 camera operating in bright field reflection mode, whilst the samples were immersed in 1 cm depth of DI water.

Contact Angle and Hysteresis Measurements: Apparent water contact angle measurements were performed using a contact angle goniometer (Dataphysics OCA25, Germany). A small drop was deposited on the surface, and the volume was increased to ≈10 µL, and then the water contact angle was measured, using the Dataphysics analysis software with the Laplace–Young model for sessile drops. For CA hysteresis (CAH), the drop volume of 20 µL was increased and decreased at a rate of 0.1 µL s^{-1} under video recording. The CAH fitting was performed by the Ellipse method (with a needle in), using the Dataphysics analysis software. It should be noted that the calculated values obtained by the Ellipse fitting algorithm for CAH are lower than those calculated by the Laplace–Young fitting algorithm for the apparent CA; therefore, only the difference between the advancing and receding CAs should be considered a CAH (not the absolute calculated value). All values shown in the text were averaged from at least three independent measurements.

Most Stable Contact Angle (MSCA) Measurements: Since the bulk metal surface cannot be polished to an atomically smooth topography, the MSCA values were measured on the FS-modified polished Si/SiO$_2$ substrates (μChemicals, Si(100) p-type + 100 nm SiO$_2$) with nanometer-scale roughness. Since there is no common method to determine the MSCA, the advancing and receding CAs were measured, which are the maximum and minimum apparent CA values, respectively. An apparent CA could then be any value between these two limiting values.[30] The advancing and receding WCAs were measured using a DSA100 contact angle goniometer (KRUSS, Germany) as follows: the drop of 20 µL volume was infused to the Si/SiO$_2$/FS substrates at a rate of 0.05 µL s^{-1}, the drop of 40 µL was withdrawn from Si/SiO$_2$/FS at a rate of 0.05 µL s^{-1}, and the image was recorded. The shape of a sessile drop was calculated using the Ellipse method (Tangent-1) by KRUSS Drop Shape Analysis software. All values shown in the text were averaged from at least three independent measurements. For validation, the MSCA was also obtained on polished (mirror-like) Al surfaces that were briefly anodized in an aqueous oxalic acid electrolyte to form a thin dense Al oxide layer, followed by the FS-modification (P-Al/FS).

Surface Roughness Measurements: A Park NX20 atomic force microscope (AFM, Park Systems Suwon) was used to calculate the roughness parameter of the samples. Measurements were performed in contact mode using CONTSCR contact cantilevers with low resonant frequency (25 kHz) and low spring constant (0.2 N m^{-1}). All images were acquired at a resolution of 1024 × 1024 pixels, a scan rate of 0.10 Hz, and a scan range of 20–50 µm^2. The AFM images were analyzed using Gwyddion 2.61 software, and the dimensionless roughness parameters were calculated by dividing the obtained surface area by the projected area. Statistical analysis of the roughness parameter of SHS was determined from at least three spots.

Mechanical Durability Measurements: Nanoindentation measurements were performed with a Nanoindenter XP (Keysight, USA) equipped with a diamond Berkovich tip (Synton MDP, Switzerland) and the Continuous Stiffness Measurement (CSM) option. Indents were performed to a final depth of 2000 nm. Due to the high surface roughness of the E-Al and EA-Al samples, a large field of 50 indents was performed and only indents that showed a regular load-displacement and modulus-displacement performance were used for analysis. All other experiments are deemed strongly influenced by the high surface roughness, i.e., the indenter tip hit somewhere in between the surface nanostructures. In any case, at least six indents from each investigated material state were successful and used for analyzing hardness and elastic modulus.

Potentiodynamic Polarization Measurements and Long-Term Immersion Tests: Corrosion experiments were performed in a 3.5 wt.% NaCl aqueous electrolyte with a three-electrode configuration, with the sample as

Table 2. Chemical compositions of artificial seawater.[58]

Chemical	Concentration [g L^{-1}]
NaCl	24.53
MgCl$_2$	5.20
Na$_2$SO$_4$	4.09
CaCl$_2$	1.16
KCl	0.695
NaHCO$_3$	0.201
KBr	0.101
H$_3$BO$_3$	0.027
SrCl$_2$	0.025
NaF	0.003

the working electrode, a platinum as a counter electrode, and an Ag/AgCl 3 M reference electrode. The sample was in contact with the electrolyte through a circular O-ring in the cell wall sealed by an O-ring of 10 mm in diameter. For each sample, open-circuit potential (OCP) measurements (Zahner Zennium Electrochemical Workstation) were made until a stable OCP value was reached; then a potentiodynamic polarization was performed from −100 mV versus the OCP until 1.50 V versus the reference electrode at a scan rate of 1 mV s^{-1}. The long-term corrosion resistance measurements were performed by the immersion of bare, etched, and etched/anodized Al substrates in an artificial seawater medium in a Petri dish at ambient atmosphere. The composition of the artificial seawater is summarized in **Table 2**. The digital and the bright-field optical microscopy images were taken each week of immersion, whilst the bright-field optical microscopy images were taken after 5 weeks of immersion and then were returned to aquatic media for further evaluation of corrosion resistance longevity.

Electrochemical Impedance Spectroscopy Measurements: Electrochemical impedance spectroscopy (EIS) measurements were performed in a borate aqueous electrolyte (0.075 M Na$_2$B$_4$O$_7$·10H$_2$O, and 0.3 M H$_3$BO$_3$, pH 8.4) with a three-electrode configuration, where the sample was used as the working electrode, a platinum electrode as a counter electrode, with a HydroFlex reversible hydrogen reference electrode. The sample was in contact with the electrolyte through a circular O-ring sealed opening in the cell wall exposing a circular area of 10 mm in diameter. For each sample, open circuit potential (OCP) measurements (Zahner Zennium Electrochemical Workstation) were taken for ≈1 h until a stable OCP value was reached. EIS measurements were performed in the frequency range between 10 mHz and 100 kHz with a 10 mV amplitude sinusoidal voltage. Equivalent circuit simulations and fitting of the measured data were performed using the EISanalyzer software.[59]

Supporting Information

Supporting Information is available from the Wiley Online Library or from the author.

Acknowledgements

Conflict of Interest

The authors declare no conflict of interest.

Data Availability Statement

The data that support the findings of this study are available from the corresponding author upon reasonable request.

Keywords

[1] Q. Schiermeier, J. Tollefson, T. Scully, A. Witze, O. Morton, *Nature.* **2008**, *454*, 816.

[2] L. Xu, T. Jiang, P. Lin, J. J. Shao, C. He, W. Zhong, X. Y. Chen, Z. L. Wang, *ACS Nano.* **2018**, *12*, 1849.

[3] A. F. d. O. Falcão, *Renew. Sustainable Energy Rev.* **2010**, *14*, 899.

[4] R. Bender, D. Féron, D. Mills, S. Ritter, R. Bäßler, D. Bettge, I. De Graeve, A. Dugstad, S. Grassini, T. Hack, M. Halama, E.-H. Han, T. Harder, G. Hinds, J. Kittel, R. Krieg, C. Leygraf, L. Martinelli, A. Mol, D. Neff, J.-O. Nilsson, I. Odnevall, S. Paterson, S. Paul, T. Prošek, M. Raupach, R. I. Revilla, F. Ropital, H. Schweigart, E. Szala, et al., *Mater. Corros.* **2022**, *73*, 1730.

[5] R. M. Davison, T. R. Laurin, J. D. Redmond, H. Watanabe, M. Semchyshen, *Mater. Des.* **1986**, *7*, 111.

[6] L. Kang, C. Yang, *Adv. Eng. Mater.* **2019**, *21*, 1801359.

[7] V. V. Ramalingam, P. Ramasamy, M. D. Kovukkal, G. Myilsamy, *Metals Mater. Int.* **2020**, *26*, 409.

[8] J. Zhang, J. Miao, N. Balasubramani, D. H. Cho, T. Avey, C.-Y. Chang, A. A. Luo, *J. Magnesium Alloys.* **2023**, *11*, 3867.

[9] S. Caba, *ATZ Worldwide.* **2020**, *122*, 58.

[10] E. A. Starke, J. T. Staley, *Prog. Aerosp. Sci.* **1996**, *32*, 131.

[11] E. Georgantzia, M. Gkantou, G. S. Kamaris, *Eng. Struct.* **2021**, *227*, 111372.

[12] D. de la Fuente, E. Otero-Huerta, M. Morcillo, *Corros. Sci.* **2007**, *49*, 3134.

[13] M. A. Wahid, A. N. Siddiquee, Z. A. Khan, *Mar. Syst. Ocean Technol.* **2020**, *15*, 70.

[14] A. O. Emmanuel, O. S. I. Fayomi, I. G. Akande, *IOP Conf. Ser. Mater. Sci. Eng.* **2021**, *1107*, 012024.

[15] A. B. Tesler, T. Sannomiya, A. Vaskevich, E. Sabatani, I. Rubinstein, *Adv. Optical Mater.* **2018**, *6*, 1800599.

[16] a) Z. Szklarska-Smialowska, *Corros. Sci.* **1999**, *41*, 1743; b) P. M. Natishan, W. E. O'Grady, *J. Electrochem. Soc.* **2014**, *161*, C421; c) E. McCafferty, P. M. Natishan, *ECS Trans.* **2011**, *33*, 47.

[17] J. R. Davis, in *Corrosion of Aluminum and Aluminum Alloys* (Ed.: J. R. Davis), ASM International, Ohio, **1999**, p. 25. https://doi.org/10.31399/asm.tb.caaa.t67870025.

[18] a) N. Birbilis, R. G. Buchheit, *J. Electrochem. Soc.* **2005**, *152*, B140; b) J. Wloka, S. Virtanen, *J. Electrochem. Soc.* **2007**, *154*, C411; c) Z. Szklarska-Smialowska, *Corros. Sci.* **1992**, *33*, 1193; d) R. T. Foley, *Corrosion.* **1986**, *42*, 277.

[19] a) V. S. Sastri, in *Green Corrosion Inhibitors* (Ed.: V. S. Sastri), A John Wiley and Sons Inc., New Jersy **2011**, p. 139, https://doi.org/10.1002/9781118015438.ch4; b) M. W. Kendig, R. G. Buchheit, *Corrosion.* **2003**, *59*, 379.

[20] D. Zhang, L. Wang, H. Qian, X. Li, *J. Coat. Technol. Res.* **2016**, *13*, 11.

[21] a) Y. Liu, J. Liu, S. Li, Y. Wang, Z. Han, L. Ren, *Colloids Surf., A.* **2015**, *466*, 125; b) M. Cui, Y. Shen, H. Tian, Y. Yang, H. Feng, J. Li, *Surf. Coat. Technol.* **2018**, *347*, 38; c) X. Li, Q. Zhang, Z. Guo, T. Shi, J. Yu, M. Tang, X. Huang, *Appl. Surf. Sci.* **2015**, *342*, 76.

[22] a) A. Marmur, *Soft Matter.* **2013**, *9*, 7900; b) X.-M. Li, D. Reinhoudt, M. Crego-Calama, *Chem. Soc. Rev.* **2007**, *36*, 1350.

[23] D. J. W., B. Ludmila, C. Emil, D. V. Claudio, H. Lucyna, M. Abraham, S. Stefano, *Surf. Innov.* **2020**, *8*, 3.

[24] R. N. Wenzel, *Ind. Eng. Chem.* **1936**, *28*, 988.

[25] A. B. D. Cassie, S. Baxter, *Trans. Faraday Soc.* **1944**, *40*, 546.

[26] a) A. Lafuma, D. Quéré, *Nat. Mater.* **2003**, *2*, 457; b) R. Poetes, K. Holtzmann, K. Franze, U. Steiner, *Phys. Rev. Lett.* **2010**, *105*, 166104.

[27] A. Marmur, C. Della Volpe, S. Siboni, A. Amirfazli, J. W. Drelich, *Surf. Innov.* **2017**, *5*, 3.

[28] A. Marmur, S. Kojevnikova, *J. Colloid Interface Sci.* **2020**, *568*, 148.

[29] H.-J. Butt, J. Liu, K. Koynov, B. Straub, C. Hinduja, I. Roismann, R. Berger, X. Li, D. Vollmer, W. Steffen, M. Kappl, *Curr. Opin. Colloid Interface Sci.* **2022**, *59*, 101574.

[30] F. Chen, Y. Wang, Y. Tian, D. Zhang, J. Song, C. R. Crick, C. J. Carmalt, I. P. Parkin, Y. Lu, *Chem. Soc. Rev.* **2022**, *51*, 8476.

[31] M. Nosonovsky, B. Bhushan, *Microsyst. Technol.* **2006**, *12*, 231.

[32] a) Y. Lu, S. Sathasivam, J. Song, C. R. Crick, C. J. Carmalt, I. P. Parkin, *Science.* **2015**, *347*, 1132; b) D. Wang, Q. Sun, M. J. Hokkanen, C. Zhang, F.-Y. Lin, Q. Liu, S.-P. Zhu, T. Zhou, Q. Chang, B. He, Q. Zhou, L. Chen, Z. Wang, R. H. A. Ras, X. Deng, *Nature.* **2020**, *582*, 55; c) C. Peng, Z. Chen, M. K. Tiwari, *Nat. Mater.* **2018**, *17*, 355; d) A. B. Tesler, P. Kim, S. Kolle, C. Howell, O. Ahanotu, J. Aizenberg, *Nat. Commun.* **2015**, *6*, 8649.

[33] M. Nosonovsky, B. Bhushan, *J. Phys.: Condens. Matter.* **2008**, *20*, 225009.

[34] G. B. Hwang, K. Page, A. Patir, S. P. Nair, E. Allan, I. P. Parkin, *ACS Nano.* **2018**, *12*, 6050.

[35] K. Zheng, J. Zhang, E. Keaney, H. Dodiuk, S. Kenig, C. Barry, J. Mead, *J. Coat. Technol. Res.* **2021**, *18*, 685.

[36] a) A. B. Tesler, S. Kolle, L. H. Prado, I. Thievessen, D. Böhringer, M. Backholm, B. Karunakaran, H. A. Nurmi, M. Latikka, L. Fischer, S. Stafslien, Z. M. Cenev, J. V. I. Timonen, M. Bruns, A. Mazare, U. Lohbauer, S. Virtanen, B. Fabry, P. Schmuki, R. H. A. Ras, J. Aizenberg, W. H. Goldmann, *Nat. Mater.* **2023**, *22*, 1548; b) A. B. Tesler, H. A. Nurmi, S. Kolle, L. H. Prado, B. Karunakaran, A. Mazare, I. Erceg, I. de Brito Soares, G. Sarau, S. Christiansen, S. Stafslien, J. Alvarenga, J. Aizenberg, B. Fabry, R. H. A. Ras, W. H. Goldmann, *Commun. Mater.* **2024**, *5*, 112.

[37] a) W. Liu, L. Sun, Y. Luo, R. Wu, H. Jiang, Y. Chen, G. Zeng, Y. Liu, *Appl. Surf. Sci.* **2013**, *280*, 193; b) D. Zang, R. Zhu, W. Zhang, J. Wu, X. Yu, Y. Zhang, *Corros. Sci.* **2014**, *83*, 86; c) R. Liao, Z. Zuo, C. Guo, Y. Yuan, A. Zhuang, *Appl. Surf. Sci.* **2014**, *317*, 701; d) Y. Huang, D. K. Sarkar, X. G. Chen, *Appl. Surf. Sci.* **2015**, *356*, 1012; e) X. Zhang, J. Zhao, J. Mo, R. Sun, Z. Li, Z. Guo, *Colloids Surf., A.* **2019**, *567*, 205; f) A. Khaskhoussi, L. Calabrese, E. Proverbio, *Appl. Sci.* **2020**, *10*, 2656; g) B. Qian, Z. Shen, *Langmuir.* **2005**, *21*, 9007.

[38] a) W. Liu, Y. Luo, L. Sun, R. Wu, H. Jiang, Y. Liu, *Appl. Surf. Sci.* **2013**, *264*, 872; b) H. Zhang, L. Yin, L. Li, S. Shi, Y. Wang, X. Liu, *RSC Adv.* **2016**, *6*, 14034; c) R. Wu, S. Wu, H. Jiang, Z. Chang, Z. Yuan, Q. Chen,

Mater. Express. **2021**, *11*, 2004; d) Z. Zhang, F. Xue, W. Bai, X. Shi, Y. Liu, L. Feng, *Surf. Coat. Technol.* **2021**, *410*, 126952.

[39] a) H. Masuda, K. Fukuda, *Science.* **1995**, *268*, 1466; b) G. E. Thompson, G. C. Wood, in *Treatise on Materials Science and Technology*, Vol. 23 (Ed.: J. C. Scully), Academic Press Inc, New York **1983**, p. 205; c) S. Ono, M. Saito, H. Asoh, *Electrochim. Acta.* **2005**, *51*, 827; d) F. Li, L. Zhang, R. M. Metzger, *Chem. Mater.* **1998**, *10*, 2470; e) T. Kikuchi, D. Nakajima, O. Nishinaga, S. Natsui, R. O. Suzuki, *Curr. Nanosci.* **2015**, *11*, 560; f) H. Takahashi, M. Nagayama, *Electrochim. Acta.* **1978**, *23*, 279.

[40] a) Y. Zhang, J. Wu, X. Yu, H. Wu, *Appl. Surf. Sci.* **2011**, *257*, 7928; b) O. Adarraga, C. Agustín-Sáenz, I. Bustero, F. Brusciotti, *Sci. Rep.* **2023**, *13*, 1737.

[41] a) H.-J. Oh, J.-H. Lee, H.-J. Ahn, Y. Jeong, N.-J. Park, S.-S. Kim, C.-S. Chi, *Mater. Sci. Eng., A.* **2007**, *449–451*, 348; b) R. S. Alwitt, H. Uchi, T. R. Beck, R. C. Alkire, *J. Electrochem. Soc.* **1984**, *131*, 13.

[42] I. T. Cousins, J. H. Johansson, M. E. Salter, B. Sha, M. Scheringer, *Environ. Sci. Technol.* **2022**, *56*, 11172.

[43] a) L. H. Prado, D. Böhringer, A. Mazare, L. Sotelo, G. Sarau, S. Christiansen, B. Fabry, P. Schmuki, S. Virtanen, W. H. Goldmann, A. B. Tesler, *ACS Appl. Mater. Interfaces.* **2023**, *15*, 31776; b) E. Forrest, R. Schulze, C. Liu, D. Dombrowski, *Int. J. Heat Mass Transfer.* **2015**, *91*, 311.

[44] M. Rahimi, A. Afshari, E. Thormann, *ACS Appl. Mater. Interfaces.* **2016**, *8*, 11147.

[45] S. Wciślik, S. Mukherjee, *Phys. Fluids.* **2022**, 34.

[46] D. Cwikel, Q. Zhao, C. Liu, X. Su, A. Marmur, *Langmuir.* **2010**, *26*, 15289.

[47] A. B. Tesler, Z. Sheng, W. Lv, Y. Fan, D. Fricke, K.-C. Park, J. Alvarenga, J. Aizenberg, X. Hou, *ACS Nano.* **2020**, *14*, 2465.

[48] a) L. Assaud, S. Bochmann, S. Christiansen, J. Bachmann, *Rev. Sci. Instrum.* **2015**, *86*, 073902; b) O. Jessensky, F. Müller, U. Gösele, *Appl. Phys. Lett.* **1998**, *72*, 1173; c) A. Rauf, M. Mehmood, M. Asim Rasheed, M. Aslam, *J. Solid State Electrochem.* **2009**, *13*, 321; d) G. D. Sulka, W. J. Stępniowski, *Electrochim. Acta.* **2009**, *54*, 3683; e) L. Zaraska, W. J. Stępniowski, E. Ciepiela, G. D. Sulka, *Thin Solid Films.* **2013**, *534*, 155.

[49] Y. Yamamoto, N. Baba, *Thin Solid Films.* **1983**, *101*, 329.

[50] A. Marmur, *Langmuir.* **2006**, *22*, 1400.

[51] A. Giacomello, L. Schimmele, S. Dietrich, *Proc. Natl. Acad. Sci. USA.* **2016**, *113*, E262.

[52] S. Ko, D. Lee, S. Jee, H. Park, K. Lee, W. Hwang, *Thin Solid Films.* **2006**, *515*, 1932.

[53] Y. Ge, J. Cheng, X. Wang, L. Xue, S. Zhu, B. Zhang, S. Hong, Y. Wu, X. Zhang, X.-B. Liang, *ACS Omega.* **2021**, *6*, 18383.

[54] G. X. Shen, Y. C. Chen, L. Lin, C. J. Lin, D. Scantlebury, *Electrochim. Acta.* **2005**, *50*, 5083.

[55] A. R. C. Bredar, A. L. Chown, A. R. Burton, B. H. Farnum, *ACS App. Energy Mater.* **2020**, *3*, 66.

[56] M. Xu, G. Sun, C.-J. Kim, *Phys. Rev. Lett.* **2014**, *113*, 136103.

[57] T. Inoue, A. Koyama, D. Kowalski, C. Zhu, Y. Aoki, H. Habazaki, *Physica Status Solidi.* **2020**, *217*, 1900836.

[58] H. A. Baensch, H. Debelius, in *Meerwasser Atlas 1: Die gemeinsame Pflege von Wirbellosen Tieren und tropischen Meeresfischen im Aquarium*, Mergus-Verlag GmbH, Osnabrück **2006**.

[59] A. Bondarenko, G. Ragoisha, in *Progress in Chemometrics Research* (Ed.: A. L. Pomerantsev), Nova Science Publishers, New York **2005**, pp. 89–102.